Bioactive Materials 13 (2022) 1–8

Contents lists available at ScienceDirect

Bioactive Materials

journal homepage: www.keaipublishing.com/en/journals/bioactive-materials

PoreScript: Semi-automated pore size algorithm for scaffold characterization

Dana Jenkins [a], Karim Salhadar [a], Grant Ashby [a], Anita Mishra [a], Joy Cheshire [a], Felipe Beltran [b], Melissa Grunlan [b], Sébastien Andrieux [c], Cosima Stubenrauch [d], Elizabeth Cosgriff-Hernandez [a,*]

[a] Department of Biomedical Engineering, University of Texas – Austin, Austin, TX, 78712, USA
[b] Department of Biomedical Engineering, Texas A&M University, College Station, TX, 77843, USA
[c] Université de Strasbourg, CNRS, Institut Charles Sadron UPR22, F-67000, Strasbourg, France
[d] Institut für Physikalische Chemie, Universität Stuttgart, Pfaffenwaldring 55, D-70569, Stuttgart, Germany

ARTICLE INFO

Keywords:
Pore size measurement
Polymer scaffolds
MATLAB program
Tissue engineering

ABSTRACT

The scaffold pore size influences many critical physical aspects of tissue engineering, including tissue infiltration, biodegradation rate, and mechanical properties. Manual measurements of pore sizes from scanning electron micrographs using ImageJ/FIJI are commonly used to characterize scaffolds, but these methods are both time-consuming and subject to user bias. Current semi-automated analysis tools are limited by a lack of accessibility or limited sample size in their verification process. The work here describes the development of a new MATLAB algorithm, PoreScript, to address these limitations. The algorithm was verified using three common scaffold fabrication methods (e.g., salt leaching, gas foaming, emulsion templating) with varying pore sizes and shapes to demonstrate the versatility of this new tool. Our results demonstrate that the pore size characterization using PoreScript is comparable to manual pore size measurements. The PoreScript algorithm was further evaluated to determine the effect of user-input and image parameters (relative image magnification, pixel intensity threshold, and pore structure). Overall, this work validates the accuracy of the PoreScript algorithm across several fabrication methods and provides user-guidance for semi-automated image analysis and increased throughput of scaffold characterization.

1. Introduction

Tissue engineering scaffolds provide a framework to restore function and guide tissue regeneration. Fabrication methods (e.g., emulsion templating, gas foaming, salt leaching) provide researchers with a highly tunable design space to control scaffold geometry and microarchitecture [1–7]. The resulting pore size can range from nanometers to millimeters with either narrow or broad pore size distributions [8]. Additionally, there is a broad spectrum of pore shapes, from spherical to cubic [2,9,10]. The pore size and architecture are critical characteristics of tissue engineered scaffolds that strongly impact cell-material interactions, biodegradation and mechanical properties [8,11–15]. For example, increasing pore size has been shown to increase cellular infiltration and metabolic transport [12,14,16]. Given that scaffold microarchitecture strongly impacts regeneration outcomes, the characterization of scaffold pore size and distribution is a key determinant in the development of tissue engineering scaffolds.

Mercury porosimetry is a well-established method to characterize macroporous materials and measures the porosity of a material by applying controlled pressure to a sample immersed in mercury [17,18]. The Washburn equation is used to calculate the pore diameter which is inversely related to the pressure required for the non-wetting liquid to intrude the pores. This method can provide pore size and pore volume distribution by the pore volume of entire specimens; however, it has notable limitations in the characterization of tissue engineering scaffolds. Mercury porosimetry does not account for closed pores and does not characterize scaffold interconnectivity, strut/wall thickness, or anisotropy. Particularly important for soft tissue applications is the fact

Peer review under responsibility of KeAi Communications Co., Ltd.
* Corresponding author. 107 W. Dean Keeton, BME Building, Room 3.503D, Austin, TX, 78712, USA.
E-mail addresses: dj23245@utexas.edu (D. Jenkins), karimsalhadar@gmail.com (K. Salhadar), grantashby@utexas.edu (G. Ashby), anitamishra@utexas.edu (A. Mishra), joycheshire@utexas.edu (J. Cheshire), fbeltran@tamu.edu (F. Beltran), mgrunlan@tamu.edu (M. Grunlan), sebastien.andrieux@ics-cnrs.unistra.fr (S. Andrieux), cosima.stubenrauch@ipc.uni-stuttgart.de (C. Stubenrauch), cosgriff.hernandez@utexas.edu (E. Cosgriff-Hernandez).

https://doi.org/10.1016/j.bioactmat.2021.11.006
Received 6 August 2021; Received in revised form 11 October 2021; Accepted 4 November 2021
Available online 12 November 2021
2452-199X/© 2021 The Authors. Publishing services by Elsevier B.V. on behalf of KeAi Communications Co. Ltd. This is an open access article under the CC BY-NC-ND license (http://creativecommons.org/licenses/by-nc-nd/4.0/).

that one applies high pressures with the porosimeter (up to 400 MPa). These pressures can cause specimen collapse thus resulting in inaccurate measurements of flexible or fragile scaffolds [17]. Micro computed tomography (micro-CT) is another method used to analyze scaffold microarchitecture. Although microCT provides the full tomography of the sample, the relatively high cost and low accessibility limit its broad use [19]. Scanning electron microscopy (SEM) is the most common method to obtain representative images of the microarchitecture of the scaffold. Scanning electron micrographs are analyzed using image analysis like ImageJ/FIJI to measure pore and pore opening sizes (interconnects) manually [20–23]. However, there is no standardized protocol that provides guidance to ensure rigor and reduce user bias (e.g., pore selection method, number of pores per image and number of images per specimen). There is a trade-off between increasing the number of pores analyzed to provide an accurate quantification of the pore size distribution and the time associated with manual evaluation of SEM images.

A semi-automated system would improve manual methods by increasing the number of pore measurements per image for a more representative analysis of the specimen microarchitecture. Semi-automation would also reduce user bias in the selection of which pores to measure and. Guarino et al. developed a semi-automated MATLAB image processing method to streamline pore size analysis [24]. Their image processing approach was implemented on the PCL scaffold by using a MATLAB routine for image segmentation based on the edge detection method. However, this program requires a pre-processing step to reduce noise and smooth homogeneous regions, thus increasing overall analysis time and effort. Haeri et al. also developed an ImageJ plugin to analyze porous scaffolds. The algorithm was verified using images with tubular openings that appear 2D, which can lead to unexpected inaccuracy when analyzing images with pores at multiple planes or with higher porosities. With this limited data set it is unclear if the algorithm is accurate when analyzing images with pores on uneven surfaces or with higher porosities [25]. To date, pore measurement algorithms have difficulty with interconnected pore structures, have only been validated with a limited sample pool, or are not freely available [26–29]. Therefore, there is a need for a readily available, accurate, and robust method to increase the throughput and accuracy of pore characterization of tissue engineering scaffolds.

In this work, we developed a new algorithm, PoreScript, as a semi-automated method to determine scaffold pore size distributions from SEM images using a user-friendly, open-source MATLAB program. To validate this new semi-automated image analysis method, pore size measurements determined by PoreScript of different porous foams with a range of shapes and sizes were compared to conventional scaffold characterization. After validating the method, the impact of different user parameters on measurement accuracy was analyzed to provide user-guidance to improve the performance of the algorithm. In summary, this study challenged the accuracy and robustness of the PoreScript algorithm for the semi-automated image analysis and increased the efficiency of pore size characterization.

2. Materials and methods

To validate the robustness of the PoreScript algorithm, we evaluated three distinct scaffold fabrication methods to determine the accuracy across multiple pore sizes and shapes. Polymer scaffolds were fabricated using established salt leaching, gas foaming, and emulsion templating methods. Unless otherwise noted, all reagents were received from Sigma Aldrich.

2.1. Salt leached scaffold fabrication

Salt leached scaffolds were fabricated using the method described by Zhang et al. [30] Salt templates were prepared in 20 mL scintillation vials (I.D. = 25 mm) with sieved NaCl salt particles (10 g; ~460 ± 70 μm) manually mixed via spatula with 7.5 wt% DI water in four additions. After compacting the wet salt with a blunt glass bar, vials were sealed and centrifuged (15 min, 3220×*g*). Following, vials were opened, allowing salt templates to air dry (~1 h) and then dried *in vacuo* (room temperature; overnight; 30 in. Hg). Poly(ε-caprolactone) diacrylate (PCL-DA; M_n ~10 k g/mol) macromer precursor solutions were prepared with CH_2Cl_2 (0.15 g polymer per mL DCM) and combined with 15 vol% of photoinitiator solution (10 wt% of 2,2-dimethoxy-2-phenylacetophenone (DMP) in 1-vinyl-2-pyrrolidinone). Solutions were vortexed and cast onto salt templates (~5 mL per template). Sealed vials were sequentially centrifuged (10 min, 1260×*g*) to infuse the solution through the template, exposed to UV light (UV Transilluminator, 6 mW/cm^2, 365 nm, ~3 min) to crosslink the macromer, and then the vials were opened to air dry overnight. To extract the salt template and residual solvent, vials were soaked for five days in a water:ethanol mixture (1:1 vol:vol) with daily solution renewals, breaking vials and removing scaffolds on day two. The resulting scaffolds were air dried overnight and then dried *in vacuo* (room temperature, 4 h, 30 in. Hg). Finally, scaffolds were heat treated (~85 °C, 1 h) and allowed to cool to room temperature prior to characterization.

2.2. Gas foamed scaffold fabrication

Gas foamed scaffolds were fabricated using the method described by Andrieux et al. [31]. Briefly, a chitosan solution was prepared by dissolving 4 wt% chitosan in 1 v% acetic acid with magnetic stirring for 2 h. Scaffold generation was carried out using a commercial glass chip (Dolomite Microfluidics). Gas flow was pressure driven with an OB1 Mk2 Pressure Controller from Elveflow connected to a nitrogen tap. Nitrogen with traces of perfluorohexane was used as the gas phase to hinder Ostwald ripening. The chitosan solution was injected into the microfluidic chip with a syringe pump (Pump 11 Elite, Harvard Apparatus) at a controlled flow rate. Genipin was dissolved in a 1 vol% acetic acid solution. The surfactant Plantacare 2000 UP was added to a concentration of 0.1 wt% in the chitosan and genipin solutions. The chitosan and genipin solutions were mixed after bubble formation via microfluidics to initiate cross-linking.

2.3. Emulsion templated scaffold fabrication

Polymerized high internal phase emulsions (polyHIPE) were prepared following a method adapted from our previous work [32]. Polyglycerol polyricinoleate (PGPR 4125) was donated by Palsgaard. Monomers used for the organic phase included neopentyl glycol diacrylate (NGDA), NGDA with 10 mol%1,4-butanedithiol (BDT), ethylene glycol dimethacrylate (EGDMA), and butanediol dimethacrylate (BDMA). Briefly, the monomer was mixed with 10 wt% PGPR surfactant and either with 1 wt% benzoyl peroxide (BPO) as an initiator or with 1 wt% trimethylaniline (TMA) as a reducing agent. Pickering emulsions included in the study were stabilized with 8.5% hydroxyapatite or silica nanoparticles as emulsifiers in place of surfactant. After mixing the organic phase, an aqueous calcium chloride solution (1 wt%) was added to the organic phase (75 vol%) in three additions and mixed at 500 rpm for 2.5 min each to promote emulsification. The two HIPEs (BPO and TMA) were mixed with a double barrel syringe and mixing head to initiate crosslinking. The HIPEs were transferred to 2-mL microcentrifuge tubes and placed in a 37 °C aluminum bead bath to facilitate crosslinking overnight.

2.4. Pore architecture characterization

Scanning electron microscopy (SEM) was utilized to image each of the scaffold architectures. Scaffolds were dried, sectioned, and sputter-coated before characterization. Salt-leached scaffolds were freeze-fractured in liquid nitrogen and were imaged with a JEOL 6400 SEM after coating with Au–Pt. Gas foamed scaffolds were freeze-fractured in

liquid nitrogen, sputtered-coated with gold, and then imaged with a CamScan CS 44. Emulsion templated scaffolds were fractured at room temperature and imaged using Phenom Pro FE-SEM after coating with gold. All samples were imaged at three different magnifications in triplicate at each magnification, Table 1. Salt leached scaffold images were taken from 27x to 110x magnifications, gas foamed scaffold images were taken from 10x to 50x magnifications, and emulsion templated scaffolds were imaged from 225x to 1000x magnifications.

2.5. Manual pore size measurements

Manual calculations of the pore sizes were conducted using open-sourced ImageJ/FIJI of SEM images to according to conventional pore size characterization methods [2,10,32]. The first ten pores along the image median were measured across their largest width to minimize user bias. If there were fewer than ten pores along the median line, the first ten pores were counted on two equidistant lines across starting from the top line down. The measured pore sizes in pixels were then multiplied by the length of the scale bar to convert to microns. Depending on the architecture of the scaffold, a correction factor was applied to account for the geometry of the scaffold architecture. Gas-foamed scaffolds had a rhombic dodecahedron structure, and thus the pore size was corrected as described by Andrieux et al. [31] For emulsion-templated scaffolds, a statistical correction value, h, was applied to account for non-perfect spherical pores, $h^2 = R^2 - r^2$, where R is the pore diameter's equatorial value, r is the diameter value measured from the micrograph, and 'h' is the distance from the center [33]. No correction factor was applied to salt-leached scaffolds due to their cubic shape. Each scaffold was evaluated at three different magnifications with three images per magnification.

2.6. PoreScript pore size measurements

PoreScript was written with the MATLAB R2019b® software. The script is based on the work of Rabbani et al. [34] The program maps pores and measures pore sizes to calculate an average pore size for individual SEM images. File type, bit depth, and the dimension of the grayscale images used here are outlined in SI Table 2. Note that we used TIFF files but that other file types (i.e. JPEG) can be used as well (see instructions in the PoreScript on how to make the algorithm compatible with other file types). Adjustable thresholds have been added to this code to improve pore identification and average pore size calculation. Adjustable thresholds have been added to this code to improve pore identification and average pore size calculation. The script consists of a user interface, a function for identifying relative pixel intensity, and a function for the pore size calculations. The output consists of three image maps, a histogram of the calculated pore diameters, and a spreadsheet. The number of pores measured in each image varied because the PoreScript evaluated the pore sizes of all the pores identified by the algorithm. The output images include a depth map, a binary segmentation map, and a pore space segmentation map. The spreadsheet contains the calculated values for the pore diameter of each pore, the average pore diameter, and the standard deviation of the pore diameter. Full details of the algorithm work flow are included in the supplemental information and are illustrated in Fig. 1. The average pore size values determined by manual and semi-automated methods were compared by plotting data pairs and fitting with a linear regression trendline.

2.7. Pore-to-image (PI) size ratio

An average pore-to-image (PI) size ratio was established to compare images of various magnifications and pore sizes, Table S1. The pixel length of each image was measured using ImageJ/FIJI. The average pore size of each image was determined as described previously. The PI ratio was then calculated by dividing the average pore size by the entire image length for each image.

2.8. Pixel intensity threshold (K)

The user manually chooses the pixel intensity threshold (K value) before analyzing a set of images to define the minimum brightness evaluated. All K values used in analysis are recorded in Table S1. The K value identifies the border between pores by testing the relative differences in pixel intensity value to neighboring cells at an adjustable percent difference value. The smaller the percent difference value, the more sensitive the finder is to differences in pixel intensity. The intensity threshold is an adjustable grey filter, K, on a scale of 0–255, where zero is black, and 255 is the brightest pixel value. This threshold is used to filter grey areas in the image into dark and bright, assuming that darker regions are lower in elevation (pore spaces). In comparison, brighter areas are higher in elevation (pore borders). Any pixel below the K value is set to zero (black), while pixels with intensity values above K are left unchanged. The modified image was then used for the pore size calculating function. To determine the pixel intensity threshold effect,

Table 1
Summary of the average pore size, total pore count (n), absolute difference, and p values when comparing manual and semi-automatic pore size measurements.

Scaffold Type	SEM Magnification	Average Manual Pore Size (μm)	Manual Total Pore Count (n)	Average PoreScript Pore Size (μm)	Pore Script Total Pore Count (n)	Absolute Difference (%)	Absolute Difference (μm)	P Value
Emulsion	800	111 ± 57	30	71 ± 40	70	36	40	0.6625
Templated (ET)	500	96 ± 43	30	84 ± 45	175	13	12	0.3304
BDMA	250	97 ± 44	30	101 ± 49	259	4	4	0.0004
ET NGDA	800	53 ± 25	30	54 ± 26	87	3	2	0.4644
	500	74 ± 40	30	63 ± 29	170	15	11	0.0717
	250	106 ± 46	30	100 ± 41	291	5	6	0.7632
ET NGDABDT	800	82 ± 50	30	60 ± 33	139	26	22	0.8064
	500	90 ± 43	30	65 ± 31	179	28	25	0.0277
	250	110 ± 58	30	94 ± 50	317	14	15	0.0380
ET BDMA nSi	1000	67 ± 25	30	58 ± 17	73	13	9	0.0901
	500	64 ± 22	30	74 ± 26	193	16	10	0.0901
	250	81 ± 24	30	69 ± 30	377	16	13	0.0803
ET NGDABDT nHA	1000	82 ± 70	30	38 ± 23	56	53	44	0.0001
	500	89 ± 65	30	69 ± 29	34	23	21	0.0965
	225	187 ± 216	30	100 ± 67	195	47	87	<0.0001
Salt Leached	110	219 ± 22	30	211 ± 22	12	4	8	0.0915
	44	217 ± 27	30	199 ± 19	76	8	17	0.0009
	27	226 ± 32	30	216 ± 29	198	5	10	0.6162
Gas Foamed	50	224 ± 15	30	216 ± 18	123	4	8	0.8064
	20	226 ± 25	30	245 ± 45	91	8	19	0.0277
	10	222 ± 26	30	220 ± 33	164	1	2	0.0380

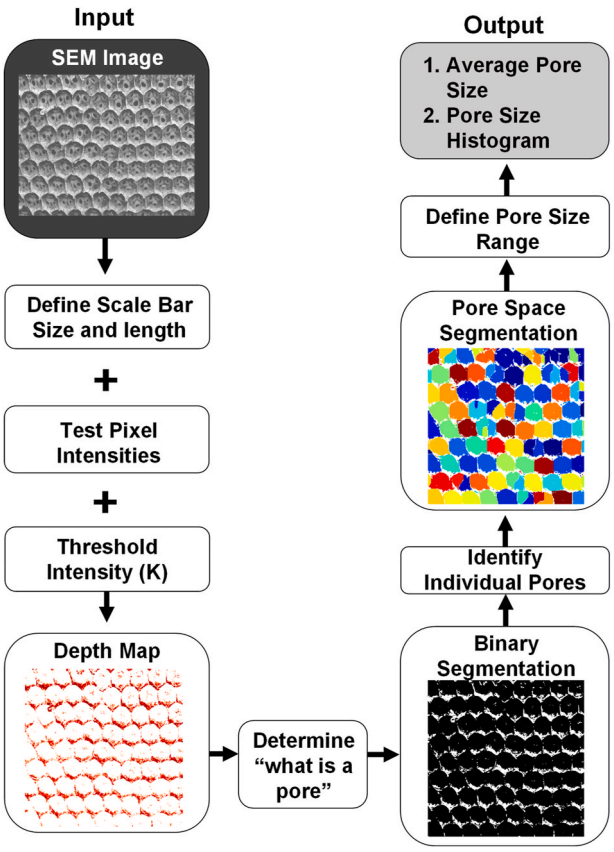

Fig. 1. Schematic illustrating the PoreScript algorithm. The input is an SEM image and the corollary outputs are a pore size histogram, an average pore diameter, and a standard deviation for each input image.

NGDABDT emulsion templated scaffolds were analyzed as a representative scaffold at a PI ratio of 0.21 (n = 3). K values were set to 130, 170, and 210. Pore sizes for manual and semi-automated analysis were then determined as described previously.

2.9. Statistical analysis

The mean ± standard deviation was reported for each set of scaffolds. A two-way student t-test was used to compare manual and semi-automatic pore size averages. Linear regression was used to determine the linear fit of the averages of three images of each group at each magnification calculated by manual or semi-automatic measurements. One-way analysis of variance (ANOVA) was used in the statistical analysis, and a Tukey post hoc test was used to assess statistical significance. $P < 0.05$ was used to determine statistical significance.

3. Results

A complete report on scaffold parameters with associated averages and sample sizes for manual and pore script analyses is provided in Table 1. A comparison of the average pore size obtained from the manual measurement data set and the semi-automated data set was used to validate the algorithm (Fig. 2). The manual method is based on the average of 10 pore size measurements per image (Fig. 2A). The PoreScript provides measurements of most pores in each image as indicated by their coloration (Fig. 2B). Average pore size was calculated for each of the seven scaffold formulations at three magnifications each for a total of 21 pore size averages for each of the two methods. This data set provided a rigorous training set to validate the PoreScript algorithm across multiple scaffold parameters, including pore size and geometry, in comparison to manual measurements. Manual and PoreScript data pairs were plotted and fit with a linear regression trendline. Perfect agreement between manual and semi-automated measurements would result in an $R^2 = 1$ and an equation of $Y = X$. The data with linear regression assessment revealed an $R^2 = 0.8985$ with an equation of $Y = 1.001X-15.080$, suggesting a strong linear correlation between the two methods (Fig. 2C). As such, this indicates that the PoreScript can be used to rapidly characterize specimens and obtain similar results to the time-intensive ImageJ method.

3.1. Effect of pore-to-image size ratio

To provide user guidance on algorithm use to optimize accuracy, the effect of user parameters was assessed. First, the effect of pore-to-image size (PI) ratio on the accuracy of pore size measurements was determined. The PI ratio was determined by dividing the average pixel length of a pore by the pixel length of the entire image. The PI ratio provides guidance to select magnifications that optimize pore size measurement accuracy for a broad range of scaffold pore sizes. Image sets were binned into low (0.02–0.12) and high (0.14–0.29) PI ratio ranges to determine its effect on measurement accuracy. Representative images across the

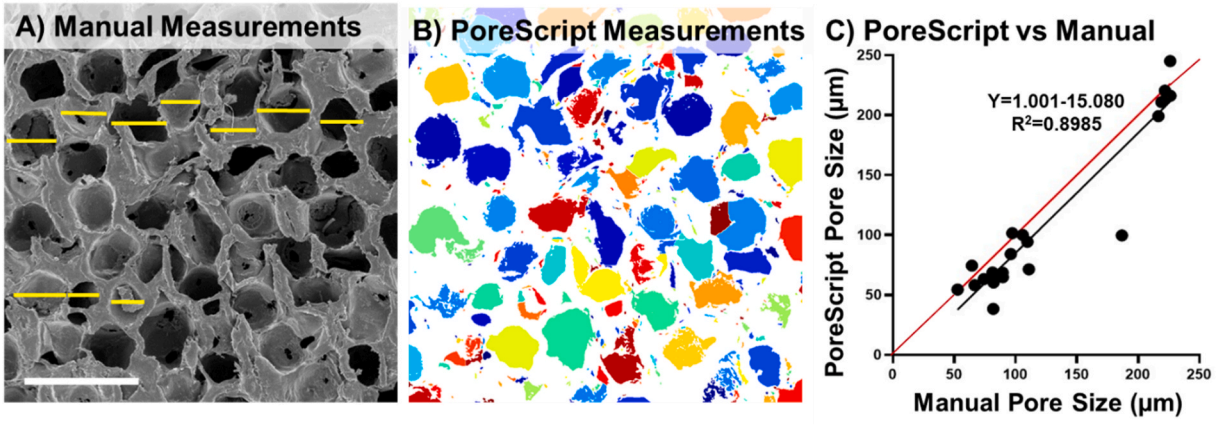

Fig. 2. Validation of PoreScript algorithm using established manual pore size measurements. Representative images (Salt-Leached, 110x, PI = 0.20) of the original SEM image with manual measurements denoted (A) and pores identified by the algorithm (B). PoreScript measurements demonstrated a near linear fit to the manually counted data (C). Unity line (red) plotted to compare to linear regression trendline of data pairs to visualize the relationship between manual and PoreScript measurements. Scale bar is 500 μm. (For interpretation of the references to color in this figure legend, the reader is referred to the Web version of this article.)

two ranges are displayed in Fig. 3A. Images with a low PI demonstrated a stronger correlation between pore size averages determined with the semi-automated method and manually, respectively, counted with an $R^2 = 0.9764$ with Y = 1.017X-7.877 (Fig. 3B). In comparison, images with a high PI ratio led to an $R^2 = 0.7410$ with Y = 0.7905X-1.393 (Fig. 3C). A strong linear correlation between the two methods was interpreted to indicate that there is good agreement with traditional manual measurements. This indicates that we can use the PoreScript to characterize specimens that would previously have been analyzed with the time-intensive ImageJ measurements based on the linear regression values, images with a low PI resulted in a more accurate average pore size as determined by the PoreScript algorithm.

3.2. Effect of pixel intensity threshold (K)

The PoreScript algorithm identifies pores based on pixel intensity contrast between a pore and areas/edges around the pore. The effect of this K value selection on pore size measurements was assessed, as seen in Fig. 4. The algorithm was run on the same three SEM images at a range of K values and the resulting average pore size measurements compared. There was no significant difference between the manual pore size averages and the PoreScript measurements at various K values ($p > 0.05$); however, there was a notable increase in the pore size distribution with increasing K value. The change in pore size distribution is most likely due to the tendency of the PoreScript to misidentify smaller pores into one larger pore at increasing K values. Thus, it is important to determine the appropriate K value for each scaffold formulation to limit misidentification of pores before analyzing data with PoreScript.

3.3. Effect of pore architecture

Finally, the effect of scaffold pore architecture on pore size measurements was determined. Salt leached, gas foamed, and emulsion templated scaffolds provided comparisons of distinct architectures to test the robustness of the algorithm (Fig. 5A). There were no significant differences between the manual and PoreScript measured pore sizes

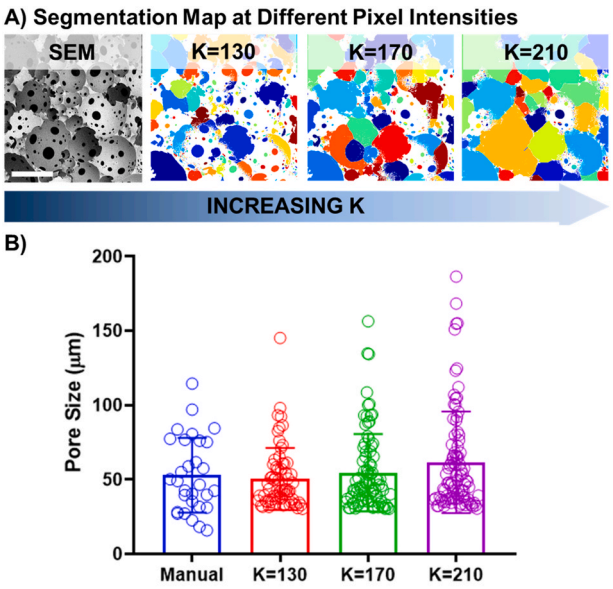

Fig. 4. Effect of pixel intensity threshold, K, on pore identification and resulting effect on pore sizes. Representative SEM image of ET NGDA (500x, PI = 0.12) analyzed at three different K values (A). Resulting pore sizes determined for three different SEM images reported (B). There was no significant difference between groups ($p > 0.05$). Scale bar is 100 µm.

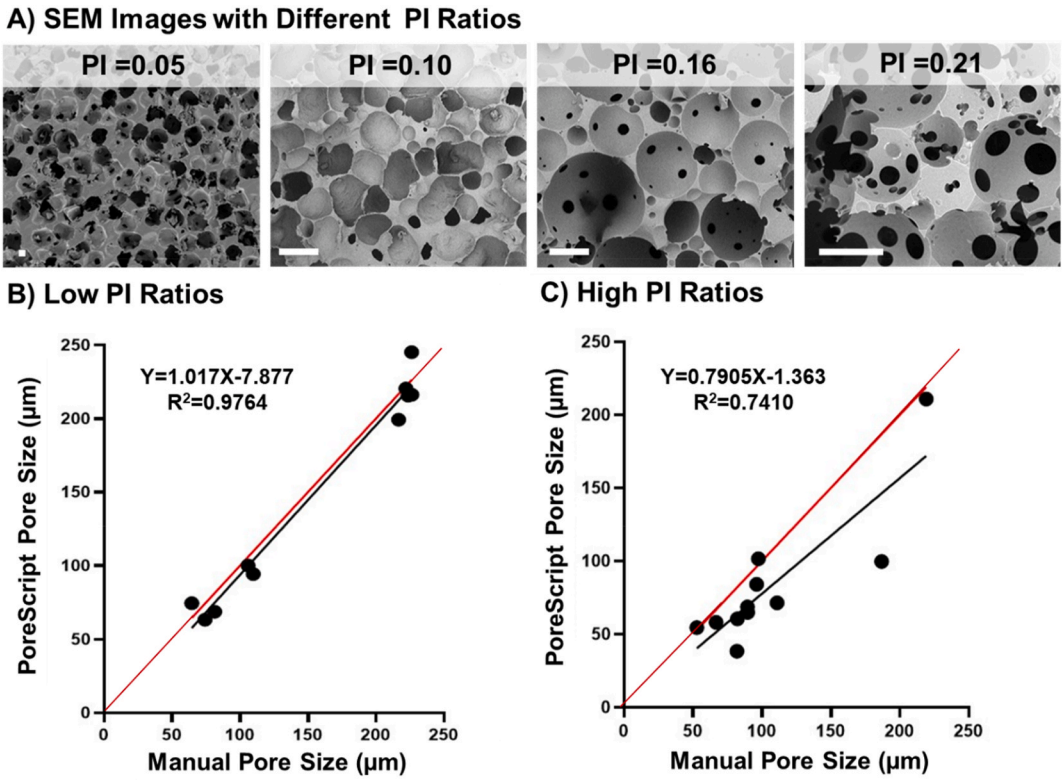

Fig. 3. The effect of pore-to-image size ratio on pore size averages. Representative SEM images with representative PI ratios of 0.05 (Salt-Leached, 27x), 0.10 (ET BDMA nSi, 500x), 0.16 (ET NGDA, 500x), and 0.21 (ET NGDABDT, 800x) (A). Low PI ratios (0.02–0.12) (B) and high PI ratios (0.14–0.29) (C) were grouped and evaluated. Unity line (red) plotted to compare to linear regression trendline of data pairs to visualize the relationship between manual and PoreScript measurements. All scale bars are 100 µm. (For interpretation of the references to color in this figure legend, the reader is referred to the Web version of this article.)

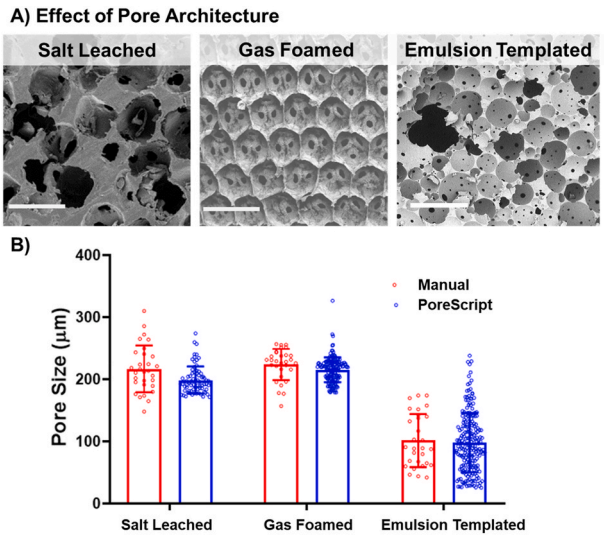

Fig. 5. Effect of pore shape and regularity on the PoreScript average pore size calculations. SEM images of salt leached (44x), gas foamed (50x), and emulsion template (NGDABDT at 250x) scaffolds at similar low PI ratios, at 0.08, 0.09 and 0.09, respectively (A). Individual and average ± standard deviations pore sizes are reported. There was no significant difference between manual and PoreScript pore size measurements ($p > 0.05$) (B). All scale bars are 300 µm.

across the different scaffold architectures (Fig. 5B). Salt leached scaffolds have irregular pore architecture and had a manual pore size average of 217 ± 27 µm and a PoreScript pore size average of 199 ± 19 µm. Gas foamed scaffolds are more regular with pores that are more hexagonal than spherical in shape and had a manual pore size average of 224 ± 15 µm and a PoreScript pore size average of 216 ± 18 µm. Emulsion templated scaffolds are more regular and spherical in shape and had a manual pore size average of 106 ± 46 µm and a PoreScript pore size average of 100 ± 41 µm. These results suggest that different pore architectures can be reliably measured using the PoreScript algorithm.

4. Discussion

This work aimed to develop and validate a semi-automated SEM image analysis method to increase the throughput of scaffold characterization. To this end, the MATLAB-based algorithm, PoreScript, was validated using SEM images of seven different polymer scaffolds generated via three different templating routes at three magnifications each. This provided a robust training set to determine the effect of multiple scaffold parameters including pore size, architecture, and magnification on measurement accuracy as compared to manual measurements. The PoreScript analysis method has several advantages compared to manual methods, including speed, reliability, and reduced user bias. The most common manual method using ImageJ requires a user to measure each pore in a single image sample. PoreScript is a three-step process for an entire SEM image set, including selecting pixel intensity threshold (K), defining the scale bar, and determining the pore size range.

To further investigate how to optimize measurements from PoreScript, we evaluated the effects of relative pore size, selection of pixel intensity, and pore architecture. Relative pore size was determined with our established PI ratio. The PI ratio was determined using the average pore size in pixel compared to total image length, with 0 being no pores in the image and 1 being one pore in an image. The images evaluated here were between 0.05 and 0.29 PI. We found that images with a lower PI ratio (0.05–0.14) overall had improved accuracy of PoreScript measurements compared to manual measurements. In contrast, images with high PI ratios (0.14–0.29) were less accurate, especially when the SEM images had pores at noticeable different focus planes (example Fig. 3A image of PI = 0.21). Although the PI ratio is not a standard measurement, an easy rule of thumb is to use micrographs with six or more pores side-by-side along the length of the image.

There are two points when using the PoreScript algorithm that can introduce user bias: 1) defining the pore size range and 2) defining the K value. The user-defined pore size range has a relatively small effect on the output if a user selects a broad size range. The pore size ranges were determined by a simple visual approximation based on the scale bar and the image, Table S1. In general, the ranges were liberal in size to allow the most pores to be correctly identified. Ranges were typically defined by the maximum being 10-fold of the minimum pore size for all samples. One could also determine the pore size range based on historical data. If a user specifies a large pore size range, there should not be minimal differences between users. Determination of the K value is another critical parameter specified by the user. In part, the PoreScript algorithm identifies pores by determining "lower elevations" or darker areas in the image. The K value is the minimum threshold of pixel darkness that the algorithm uses to identify pore versus non-pore areas. Although the selected K value ranges selected in this study did not result in statistical differences in pore measurements, it should be noted that the pore size distribution increased as the K value increased. At a low contrast ratio, the algorithm will have difficulty accurately identifying pores in the image and the range of K values that the user can use will be limited. Thus, users should aim to use high contrast images for pore size measurements. Users can then tune the K value to achieve more accurate results with the consideration that this may reduce the total number of pores analyzed in the images. Throughout this work, all images were analyzed using a K value between 100 and 200. When optimizing the K value for a data set, it is recommended to start at 150 and then increase or decrease by 20 until the Pore Segmentation Map highlights distinct individual pores.

The final variable evaluated in this work was the effect of pore architecture on the accuracy of the PoreScript. In this work, three different types of polymer scaffolds were investigated with distinct pore architecture: salt leached, gas foamed, and emulsion templated polymer scaffolds. Images were selected at a similar low PI ratio (0.08–0.09) to reduce the impact of other parameters. All PoreScript measurements were slightly lower than manual measurements, but not statistically different. The gas foamed scaffolds were the most accurate, most likely due to pores focused on the same plane. It was noted that the accuracy of PoreScript noticeably decreased when there is a significant difference between pore brightness, as seen in Fig. 6. Pores with high pixel brightness are not included in measurements. PoreScript recognizes pores by assuming that pores are darker than non-pore areas. When pores are brighter than non-pore areas, it excludes the pore, which can affect the accuracy of the measurement.

Overall, the PoreScript MATLAB algorithm offers an open-source,

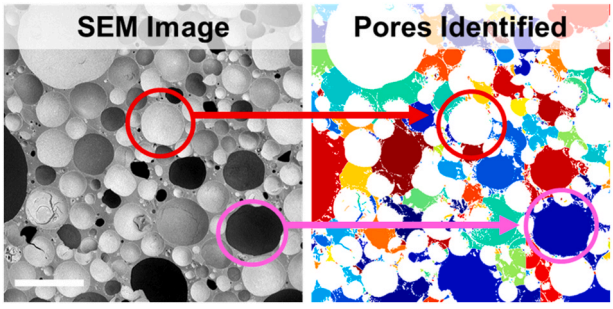

Fig. 6. Effect of pixel brightness inside and outside the pore on algorithm accuracy in pore identification. Darker pores are identified by the algorithm (pink circle); whereas lighter pores may not be identified (red circle). Scale bars is 300 µm. (For interpretation of the references to color in this figure legend, the reader is referred to the Web version of this article.)

semi-automated pore size calculator to reduce time and bias during scaffold characterization. The current work validates the measurements of several different polymer scaffolds compared to manual measurements. This work shows that it is vital to determine the appropriate PI ratio, pore size range, and K value when using the PoreScript with a new set of SEM images. Users should compare any historical data of manual pore size measurements to their PoreScript values to confirm optimal image analysis parameters. Once verified, researchers can utilize PoreScript methods for an entire set of images of a sample. Although this work was evaluated with polymeric porous scaffolds, future work should evaluate the PoreScript with other materials such as ceramic scaffolds or metallic foams.

5. Conclusion

Accurate characterization of pore size is critical in the design and testing of tissue engineering scaffolds. We developed the PoreScript algorithm to provide a semi-automated method to measure pore sizes accurately and quickly from scanning electron micrographs. The MATLAB-based method was validated using three different polymer scaffolds with distinct structures. The effects of user-defined parameters such as pixel intensity threshold and image magnification were assessed to provide useful guidelines for using the algorithm. Overall, this transition from a time-intensive manual method to a semi-automated method for measuring pore size will streamline porous material characterization and accelerate tissue scaffold development.

CRediT authorship contribution statement

Dana Jenkins: Conceptualization, MethodologyMethology, Software, Validation, Formal analysis, Investigation, Data curation, Writing – original draft, Writing – review & editing, Visualization. **Karim Salhadar:** Conceptualization, Methodology, Software, Investigation. **Grant Ashby:** Software. **Anita Mishra:** Validation, Investigation. **Joy Cheshire:** Validation, Investigation. **Felipe Beltran:** Investigation, Writing – review & editing. **Melissa Grunlan:** Writing – review & editing. **Sébastien Andrieux:** Investigation, Writing – review & editing. **Cosima Stubenrauch:** Writing – review & editing. **Elizabeth Cosgriff-Hernandez:** Conceptualization, Writing – review & editing, Visualization, Supervision, Project administration, Funding acquisition.

Declaration of competing interest

None.

Acknowledgements

The authors would like to acknowledge the following funding support: National Institutes of Health [NIH-R21 AR076708] and National Science Foundation [NSF-BSF 1822196, DGE-1610403,]. Any opinions, findings, and conclusions or recommendations expressed in this material are those of the authors and do not necessarily reflect the views of the National Science Foundation or the National Institutes of Health.

Appendix A. Supplementary data

Supplementary data to this article can be found online at https://doi.org/10.1016/j.bioactmat.2021.11.006.

Data statement

The data described in this article are openly available on Zenodo with DOI: ***10.5281/zenodo.5562953***.

References

[1] N.A. Sears, P.S. Dhavalikar, E.M. Cosgriff-Hernandez, Emulsion inks for 3D printing of high porosity materials, Macromol. Rapid Commun. 37 (16) (2016) 1369–1374.
[2] R.S. Moglia, et al., Injectable polyHIPEs as high-porosity bone grafts, Biomacromolecules 12 (10) (2011) 3621–3628.
[3] A.G. Mikos, et al., Preparation and characterization of poly (L-lactic acid) foams, Polymer 35 (5) (1994) 1068–1077.
[4] S. Andrieux, et al., Liquid foam templating–A route to tailor-made polymer foams, Adv. Colloid Interface Sci. 256 (2018) 276–290.
[5] G. Lutzweiler, et al., Modulation of Cellular Colonization of Porous Polyurethane scaffolds via the control of pore interconnection size and nanoscale surface modifications, ACS Appl. Mater. Interfaces 11 (22) (2019) 19819–19829.
[6] Y.S. Nam, J.J. Yoon, T.G. Park, A novel fabrication method of macroporous biodegradable polymer scaffolds using gas foaming salt as a porogen additive, J. Biomed. Mater. Res.: Off. J. Soc. Biomater. Japn. Soc. Biomater. Austr. Soc. Biomater. Kor. Soc. Biomater. 53 (1) (2000) 1–7.
[7] S. Zhong, Y. Zhang, C.T. Lim, Fabrication of large pores in electrospun nanofibrous scaffolds for cellular infiltration: a review, Tissue Eng. B Rev. 18 (2) (2012) 77–87.
[8] Q.L. Loh, C. Choong, Three-dimensional scaffolds for tissue engineering applications: role of porosity and pore size, Tissue Eng. B Rev. 19 (6) (2013) 485–502.
[9] S. Ahmadi, et al., Mechanical behavior of regular open-cell porous biomaterials made of diamond lattice unit cells, J. Mech. Behav. Biomed. Mater. 34 (2014) 106–115.
[10] E.M. Christenson, et al., Biodegradable fumarate-based polyHIPEs as tissue engineering scaffolds, Biomacromolecules 8 (12) (2007) 3806–3814.
[11] M. Hosseinkhani, et al., Tissue engineered scaffolds in regenerative medicine, World J. Plast. Surg. 3 (1) (2014) 3.
[12] F.M. Klenke, et al., Impact of pore size on the vascularization and osseointegration of ceramic bone substitutes in vivo, J. Biomed. Mater. Res. Part A: Off. J. Soc. Biomater. Japn. Soc. Biomater., Austr. Soc. Biomater. Kor. Soc. Biomater. 85 (3) (2008) 777–786.
[13] M.J. Gupte, et al., Pore size directs bone marrow stromal cell fate and tissue regeneration in nanofibrous macroporous scaffolds by mediating vascularization, Acta Biomater. 82 (2018) 1–11.
[14] L. Ruiz-Cantu, et al., Characterisation of the surface structure of 3D printed scaffolds for cell infiltration and surgical suturing, Biofabrication 8 (1) (2016), 015016.
[15] C.M. Murphy, M.G. Haugh, F.J. O'brien, The effect of mean pore size on cell attachment, proliferation and migration in collagen–glycosaminoglycan scaffolds for bone tissue engineering, Biomaterials 31 (3) (2010) 461–466.
[16] L. Huang, et al., Silk scaffolds with gradient pore structure and improved cell infiltration performance, Mater. Sci. Eng. C 94 (2019) 179–189.
[17] S.T. Ho, D.W. Hutmacher, A comparison of micro CT with other techniques used in the characterization of scaffolds, Biomaterials 27 (8) (2006) 1362–1376.
[18] H. Giesche, Mercury porosimetry: a general (practical) overview, Part. Part. Syst. Char. 23 (1) (2006) 9–19.
[19] S. Bertoldi, S. Farè, M.C. Tanzi, Assessment of scaffold porosity: the new route of micro-CT, J. Appl. Biomater. Biomech. 9 (3) (2011) 165–175.
[20] J. Merle, et al., New biobased foams from wood byproducts, Mater. Des. 91 (2016) 186–192.
[21] M.E. Whitely, et al., Prevention of oxygen inhibition of PolyHIPE radical polymerization using a thiol-based cross-linker, ACS Biomater. Sci. Eng. 3 (3) (2017) 409–419.
[22] R. Wu, A. Menner, A. Bismarck, Macroporous polymers made from medium internal phase emulsion templates: effect of emulsion formulation on the pore structure of polyMIPEs, Polymer 54 (21) (2013) 5511–5517.
[23] P. Habibovic, et al., 3D microenvironment as essential element for osteoinduction by biomaterials, Biomaterials 26 (17) (2005) 3565–3575.
[24] V. Guarino, et al., Image processing and fractal box counting: user-assisted method for multi-scale porous scaffold characterization, J. Mater. Sci. Mater. Med. 21 (12) (2010) 3109–3118.
[25] M. Haeri, M. Haeri, ImageJ plugin for analysis of porous scaffolds used in tissue engineering, J. Open Res. Software 3 (1) (2015) e1.
[26] G.L. Re, et al., A facile method to determine pore size distribution in porous scaffold by using image processing, Micron 76 (2015) 37–45.
[27] F.H. She, K. Tung, L. Kong, Calculation of effective pore diameters in porous filtration membranes with image analysis, Robot. Comput. Integrated Manuf. 24 (3) (2008) 427–434.
[28] E. Widiatmoko, M. Abdullah, Khairurrijal, A method to measure pore size distribution of porous materials using scanning electron microscopy images, AIP Conf. Proceed. 1284 (1) (2010) 23–26.
[29] A. Rouhollahi, O. Ilegbusi, H. Foroosh, Segmentation and pore structure estimation in SEM images of tissue engineering scaffolds using genetic algorithm, Ann. Biomed. Eng. 49 (3) (2021) 1033–1045.
[30] D. Zhang, et al., Porous inorganic–organic shape memory polymers, Polymer 53 (14) (2012) 2935–2941.
[31] S.b. Andrieux, W. Drenckhan, C. Stubenrauch, Generation of solid foams with controlled polydispersity using microfluidics, Langmuir 34 (4) (2018) 1581–1590.

[32] R.S. Moglia, et al., Injectable polymerized high internal phase emulsions with rapid in situ curing, Biomacromolecules 15 (8) (2014) 2870–2878.
[33] R.J. Carnachan, et al., Tailoring the morphology of emulsion-templated porous polymers, Soft Matter 2 (7) (2006) 608–616.
[34] A. Rabbani, S. Salehi, Dynamic modeling of the formation damage and mud cake deposition using filtration theories coupled with SEM image processing, J. Nat. Gas Sci. Eng. 42 (2017) 157–168.